Available online at www.sciencedirect.com
ScienceDirect
International Journal of Solids and Structures 43 (2006) 6277–6293
INTERNATIONAL JOURNAL OF SOLIDS and STRUCTURES
www.elsevier.com/locate/ijsolstr

Modeling of ductile fracture: Significance of void coalescence

Xiaosheng Gao *, Jinkook Kim

Department of Mechanical Engineering, The University of Akron, 302 Buchtel Mall, Akron, OH 44325, USA

Received 31 May 2005
Available online 30 September 2005

Abstract

In this paper void coalescence is regarded as the result of localization of plastic flow between enlarged voids. We obtain the failure criterion for a representative material volume (RMV) in terms of the macroscopic equivalent strain (E_c) as a function of the stress triaxiality parameter (T) and the Lode angle (θ) by conducting systematic finite element analyses of the void-containing RMV subjected to different macroscopic stress states. A series of parameter studies are conducted to examine the effects of the initial shape and volume fraction of the primary void and nucleation, growth, and coalescence of secondary voids on the predicted failure surface $E_c(T,\theta)$. As an application, a numerical approach is proposed to predict ductile crack growth in thin panels of a 2024-T3 aluminum alloy, where a porous plasticity model is used to describe the void growth process and the expression for E_c is calibrated using experimental data. The calibrated computational model is applied to predict crack extension in fracture specimens having various initial crack configurations and the numerical predictions agree very well with experimental measurements.

Keywords: Ductile crack growth; Void coalescence; Critical strain; Failure surface; Stress triaxiality; Lode angle; Void shape; Failure mode

1. Introduction

Ductile fracture of many structural materials is a result of void nucleation, growth and coalescence. Based on the fracture mechanism, a straight-forward approach to simulate ductile failure process is to model individual voids explicitly using refined finite elements, e.g., Aravas and McMeeking (1985a,b), Tvergaard and Hutchinson (2002), Kim et al. (2003), and Gao et al. (2005). A distinct advantage of this approach is the exact implementation of void growth behavior. However, due to sizeable difference between the characteristic length scales involved in the material failure process and the dimensions of the actual structural component, it is impractical to model every void in detail in structure failure analysis, especially for situations involving extensive crack propagation. For this reason, various forms of porous material models have been developed to describe void growth and the associated macroscopic softening during the fracture process. Calibration of these porous material

* Corresponding author. Tel.: +1 330 972 2415; fax: +1 330 972 6027.
E-mail address: xgao@uakron.edu (X. Gao).

0020-7683/$ - see front matter © 2005 Elsevier Ltd. All rights reserved.
doi:10.1016/j.ijsolstr.2005.08.008

models requires the predicted macroscopic stress–strain response and void growth behavior of the representative material volume (RMV) to match the results obtained from detailed finite element models with explicit void representation (Faleskog et al., 1998; Kim et al., 2004). The most widely known porous material model for analyzing ductile fracture is that due to Gurson (1977). Tvergaard (1981, 1982) modified the Gurson model by introducing two adjustment parameters to account for void interaction and material strain hardening. The Gurson–Tvergaard (GT) model assumes voids are spherical in materials and remain spherical in the growth process. But many processed materials, such as rolled plates, have non-spherical voids. And even for materials having initially spherical voids, the void shape may change to prolate or oblate, depending on the state of the applied stress. In order to overcome the limitation of the GT model, Gologanu et al. (1993, 1994, 1995) derived a yield function for materials containing spheroidal voids. In the GLD model, both void volume fraction and void shape evolve as deformation increases. Since non-spherical voids are considered in the constitutive model, preferred material orientation exists and the macroscopic plastic behavior becomes anisotropic. The GLD model returns to the Gurson model when voids become spherical. Pardoen and Hutchinson (2000, 2003), Benzerga (2002), Benzerga et al. (2004), and Kim and Gao (2005) recently implemented the GLD model into finite element analysis and their results show the computational approach based on the GLD model provides a promising tool to predict ductile material failure.

In order to simulate crack formation and propagation, a criterion for void coalescence is required. After the onset of void coalescence, material loses load carrying capacity rapidly. Comparing to the amount research conducted in modeling the void growth process, void coalescence has not received sufficient attention. A critical void volume fraction (f_c) is often used to designate the final material failure, e.g., Needleman and Tvergaard (1987), Xia et al. (1995), and Gao et al. (1998a,b). However, further studies show that f_c cannot be taken as a constant—it depends strongly on factors such as void volume fraction, void shape, void spacing, stress triaxiality, strain hardening, etc. (Benzerga et al., 1999; Zhang et al., 2000; Pardoen and Hutchinson, 2000; Kim et al., 2004). In macroscopic, the equivalent strain is often used as a measurement of material ductility. Therefore, a critical equivalent strain has also been used to denote material failure. Bao and Wierzbicki (2004a,b) and Bao (2005) conducted a series of experiments and finite element analyses on an aluminum alloy 2024-T351 and found the critical equivalent strain is a function of the stress triaxiality.

In literature, the stress triaxiality ratio (T), defined as the ratio of the mean stress to the equivalent stress, is often used as the sole parameter to characterize the effect of the triaxial stress state on ductile fracture. However, multiple stress states with different principal stress values can result in the same stress triaxiality ratio. Recent studies by Kim et al. (2003, 2004) and Gao et al. (2005) found that the macroscopic stress–strain response and the void growth and coalescence behavior of the voided RMV are different for each stress state even though the stress triaxiality ratio remains the same. Another parameter, e.g., the Lode parameter, must be introduced to distinguish the stress states having the same triaxiality ratio. In this study, we obtain the material failure criterion in terms of the critical equivalent strain (E_c) as a function of the stress triaxiality ratio (T) and the Lode angle (θ) by conducting systematic finite element analyses of the void-containing RMV subjected to different macroscopic stress states. Failure of the RMV occurs when localization of plastic flow takes place in the ligament (Koplik and Needleman, 1988). Wierzbicki and Xue (2005) recently proposed a ductile failure criterion similar to what we obtained here based on analysis of an extensive set of experimental data. Next, the effects of the initial shape and volume fraction of the primary void and nucleation, growth and coalescence of the secondary voids on the failure surface $E_c(T,\theta)$ are investigated. Finally, as an application, a numerical approach is proposed to predict ductile crack growth in thin panels of a 2024-T3 aluminum alloy, where the GLD model is used to describe the void growth process and the expression for E_c is calibrated using experimental data. The calibrated computational model is applied to predict crack extension in fracture specimens having various initial crack configurations and the numerical predictions agree very well with experimental measurements.

2. Void coalescence and material failure criterion

2.1. Macroscopic stress state of the representative material volume

Ductile fracture in metallic alloys usually follows a multistep failure process involving several interacting, simultaneous mechanisms (Van Stone et al., 1985; Garrison and Moody, 1987): (1) nucleation of microvoids

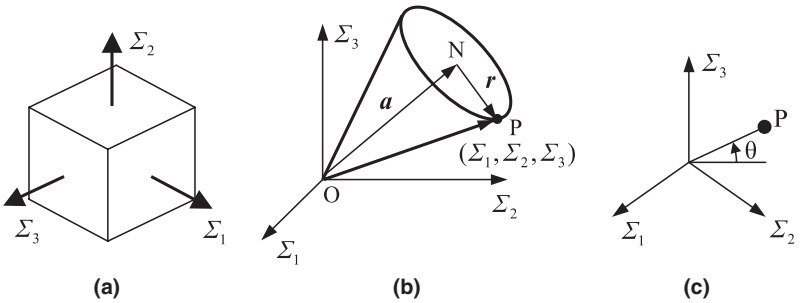

Fig. 1. (a) Stress state of a differential material volume, (b) stress states having the same stress triaxiality ratio, and (c) projection of a stress state on the π plane.

by fracture or decohesion of second-phase inclusions, (2) growth of voids induced by plastic straining, (3) localization of plastic flow between the enlarged voids, and (4) final tearing of the ligaments between enlarged voids. Nucleation of voids from large inclusions generally occurs at relatively low stress levels, and therefore, voids are often assumed to present in the material at the onset of loading. The final material separation process usually proceeds very rapidly and is often facilitated by nucleation and growth of secondary microvoids.

Assuming the existence of a periodic distribution of voids, the material can be considered as an array of cubic blocks with each block being a representative material volume (RMV) having a void at its center. The macroscopic stress–strain response and the void growth and coalescence behavior of the RMV depend sensitively on the triaxial stress state subjected by the RMV (Kim et al., 2004). In general, the RMV is subjected to a three-dimensional stress state as indicated in Fig. 1(a). Let Σ_1, Σ_2, and Σ_3 be the principal stresses and introduce the (Σ_1, Σ_2, Σ_3) coordinate system. Consider a line ON passing through the origin and having equal angles with the coordinate axes. Then every point on this line corresponds to a hydrostatic stress state. The plane passing through the origin and perpendicular to ON is called the π plane and the hydrostatic stress is zero on this plane. Consider an arbitrary stress state at point P with stress components Σ_1, Σ_2, and Σ_3. The stress vector $\vec{OP}$ can be decomposed into two components, the component $\vec{a}$ parallel to ON and the component $\vec{r}$ perpendicular to ON, where

$$a = \sqrt{3}\Sigma_{\mathrm{h}} \quad \text{and} \quad r = \sqrt{\frac{2}{3}}\Sigma_{\mathrm{e}}, \tag{1}$$

where Σ_{h} and Σ_{e} represent the hydrostatic stress and the equivalent stress, respectively. Consequently, the stress triaxiality ratio is

$$T = \frac{\Sigma_{\mathrm{h}}}{\Sigma_{\mathrm{e}}} = \frac{\sqrt{2}}{3}\frac{a}{r}. \tag{2}$$

Therefore, for a given stress triaxiality ratio T, there exist infinite number of stress states, each corresponds to a point on the surface of a cone with ON as the axis, Fig. 1(b).

It is well known that stress triaxiality has significant effect on material ductility. In literature, T is often used to characterize the effect of the triaxial stress state on ductile fracture. However, recent studies by Kim et al. (2003, 2004) and Gao et al. (2005) found that the macroscopic stress–strain response and the void growth and coalescence behavior of the voided RMV are not the same for different stress states having the same stress triaxiality ratio. To distinguish these stress states having the same T-value, consider the location on the π plane of the projection of point P, Fig. 1(c). The angles between the projections of the coordinate axes Σ_1, Σ_2, and Σ_3 on the π plane are 120°. Let θ be the angle measured from the horizontal axis, then

$$\tan\theta = \frac{2\Sigma_3 - \Sigma_2 - \Sigma_1}{\sqrt{3}(\Sigma_2 - \Sigma_1)}. \tag{3}$$

The stress triaxiality ratio (T) together with the Lode angle (θ) can be used to specify the triaxial stress state.

2.2. Void coalescence as the result of localization of plastic flow

Consider a RMV containing a void at its center and subjected to the macroscopic stresses Σ_1, Σ_2, and Σ_3. For given values of the stress triaxiality ratio, T, and the Lode angle, θ, the principal stress ratios, $\rho_1 = \Sigma_1/\Sigma_2$ and $\rho_2 = \Sigma_3/\Sigma_2$, can be determined uniquely. Therefore, in order to maintain the same values of T and θ during the entire deformation history, boundary conditions must be prescribed such that the values of ρ_1 and ρ_2 remain constants. Faleskog et al. (1998) and Kim et al. (2004) provide details of how to prescribe such boundary conditions. Here, the numerical analyses are carried out using the finite element program ABAQUS (2004), which employs a finite strain, J_2 plasticity theory within an updated Lagrangian formulation. Displacement boundary conditions are prescribed on the outer surfaces of the RMV by using the MPC user subroutine to keep the macroscopic stress ratios ρ_1 and ρ_2 constants during the loading history.

The material obeys a power-law hardening, true stress–strain relation as follows

$$\begin{aligned} \varepsilon &= \frac{\sigma}{E} \quad \sigma \leqslant \sigma_0, \\ \varepsilon &= \frac{\sigma_0}{E}\left(\frac{\sigma}{\sigma_0}\right)^{1/N} \quad \sigma > \sigma_0. \end{aligned} \tag{4}$$

Here, the material parameters are taken to be $E = 70.4$ GPa, $\sigma_0 = 345$ MPa, $v = 0.3$, and $N = 0.14$, representing a typical aluminum alloy. This power-law hardening relation is implemented in ABAQUS by using the UHARD user subroutine.

Fig. 2(a) shows a 1/8-symmetric finite element model for a cubic RMV containing a spherical void. An axisymmetric loading is considered first, where $\Sigma_2 \geqslant \Sigma_1 = \Sigma_3$ ($\theta = -30°$). The initial void volume fraction is taken as $f_0 = 0.02$. Fig. 2(b) shows the deformed shape of the RMV. Let X_0 be the initial width of the RMV in the x-direction and X be the deformed width. Fig. 3(a) shows the variation of X with the macroscopic effective strain of the RMV. As loading continues, X gradually decreases. But when the deformation reaches a certain level, X stops decreasing and remains at a constant value. This implies that further deformation takes place in a uniaxial straining mode, which corresponds to flow localization in the ligament between adjacent voids. The shift to a macroscopic uniaxial strain state indicates the onset of void coalescence. We use E_c to denote the macroscopic effective strain at the onset of void coalescence.

The macroscopic effective stress versus effective strain curve, Fig. 3(b), provides an overview of the competition between matrix material strain hardening and porosity induced softening. As deformation progresses, a maximum effective stress is reached (indicated by the filled circle), and then Σ_e decreases as strain-hardening of matrix material is insufficient to compensate for the reduction in ligament area caused by void growth. As the macroscopic effective strain reaches E_c (indicated by the open circle), a rapid drop in macroscopic effective stress occurs. As expected, both the peak stress value and the value of E_c decrease with the stress triaxiality ratio T, reflecting the decease of ductility.

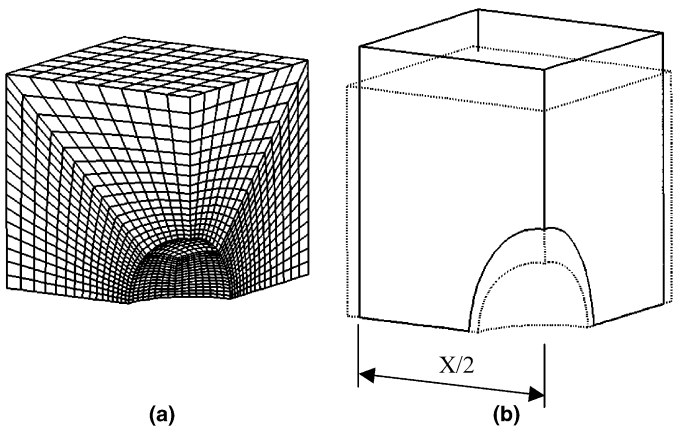

Fig. 2. (a) A 1/8-symmetric finite element mesh and (b) the deformed shape for a RMV containing a centered, spherical void.

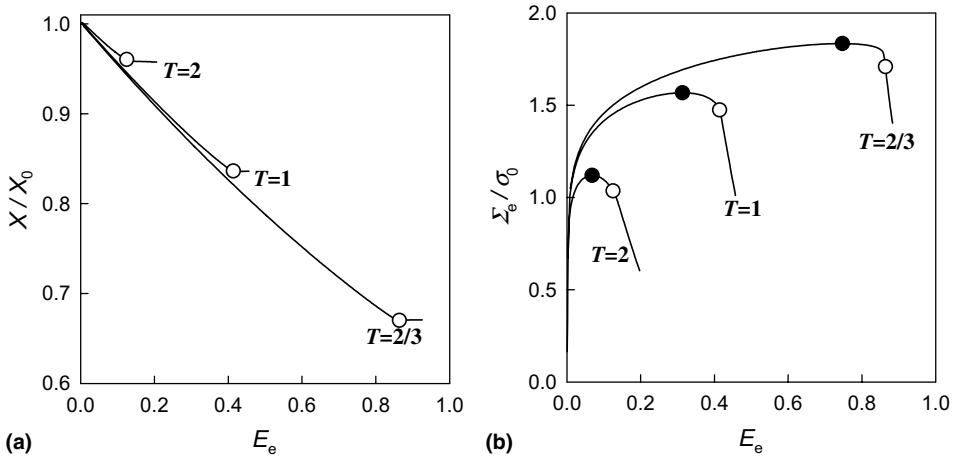

Fig. 3. (a) Variation of the deformed cell width in x-direction with the macroscopic effective strain of the cell revealing the shift to uniaxial straining. (b) Macroscopic effective stress versus effective strain of the cell displaying the macroscopic softening. Here, the applied loading is axisymmetric, i.e., $\Sigma_2 \geqslant \Sigma_1 = \Sigma_3$ ($\theta = -30°$) and the initial void volume fraction is $f_0 = 0.02$.

2.3. Effect of secondary voids on coalescence

Most engineering materials contain more than one populations of inclusions and/or second phase particles. During the void coalescence process, secondary voids nucleate in the ligament between enlarged primary voids and rapid growth and coalescence of these secondary voids accelerates the final ligament separation. Faleskog and Shih (1997) conducted 2D analysis of void coalescence where both primary and secondary voids are represented using refined finite element mesh. Here, we assume nucleation of the secondary voids is plastic strain controlled and the nucleated voids are smeared in the material. It is further assumed that void nucleation follows a normal distribution as suggested by Chu and Needleman (1980). The rate of increase of void volume fraction due to nucleation of secondary voids is given by

$$\dot{f}_{\text{nucleation}} = D\dot{\bar{\varepsilon}}, \tag{5}$$

where

$$D = \frac{f_{\text{N}}}{s_{\text{N}}\sqrt{2\pi}} \exp\left[-\frac{1}{2}\left(\frac{\bar{\varepsilon} - \varepsilon_{\text{N}}}{s_{\text{N}}}\right)^2\right]. \tag{6}$$

In above equations, $\bar{\varepsilon}$ represents the matrix plastic strain and the void nucleation parameters are chosen as $f_{\text{N}} = 0.04$, $\varepsilon_{\text{N}} = 0.1$, and $s_{\text{N}} = 0.05$. The parameters adopted here are for the purpose of demonstrating the effect of secondary voids on the void coalescence process. No attempt is made to represent the actual physical values.

To account for the growth of secondary voids and its effect on material failure, the Gurson–Tvergaard constitutive model (Gurson, 1977; Tvergaard, 1981, 1982) is used to describe the material behavior, i.e.,

$$\Phi = \frac{\Sigma_{\text{e}}^2}{\bar{\sigma}^2} + 2q_1 f \cosh\left(q_2 \frac{3\Sigma_{\text{h}}}{2\bar{\sigma}}\right) - 1 - q_1^2 f^2 = 0, \tag{7}$$

where $\bar{\sigma}$ is the current flow stress of the matrix material, f defines the current void volume fraction, and q_1 and q_2 are adjustment parameters introduced by Tvergaard (1981, 1982). Here, $q_1 = 1.5$, and $q_2 = 1$ are used in the analysis. The setting of $f = 0$ recovers the yield surface for conventional J_2 flow theory with isotropic hardening. The evolution law for void volume fraction due to void growth is determined by requiring the matrix material to be plastically incompressible

$$\dot{f}_{\text{growth}} = (1 - f)\dot{E}^p_{kk}, \tag{8}$$

where $\dot{E}^p_{kk}$ is the trace of the macroscopic plastic strain rate tensor.

To take into account the coalescence of secondary voids, we employ the f^* function introduced by Tvergaard and Needleman (1984). Parameters defining the f^* function adopt the same values as used by Tvergaard and Needleman (1984).

Consider again the RMV containing a spherical void and subjected to an axisymmetric stress state, i.e., $\Sigma_2 \geqslant \Sigma_1 = \Sigma_3$ ($\theta = -30°$). Fig. 4 compares the macroscopic effective stress versus effective strain curves between models including and not including secondary voids. Here, two initial values of primary void volume fraction, $f_0 = 0.002$ and 0.02, and several values of stress triaxiality ratio, $T = 1/3$, 2/3, 1, 1.5, and 2, are considered. The open circles denote the onset of coalescence for models where secondary voids are not taken into account. The filled circles represent the onset of coalescence for models where nucleation, growth and coalescence of secondary voids are accounted for. It is clear that secondary voids significantly accelerate the void coalescence process. It is worth noting that, for cases having very low stress triaxiality, e.g., $T = 1/3$, coalescence cannot occur without secondary voids.

For fixed Lode angle ($\theta = -30°$), E_c decreases monotonically with T as shown in Fig. 5, where curves having open symbols display the results obtained from models not including secondary voids and curves having filled symbols display the results with secondary voids being considered. Fig. 5 shows that the variation of E_c versus T becomes more pronounced as T decreases and E_c becomes less sensitive to T when T is large.

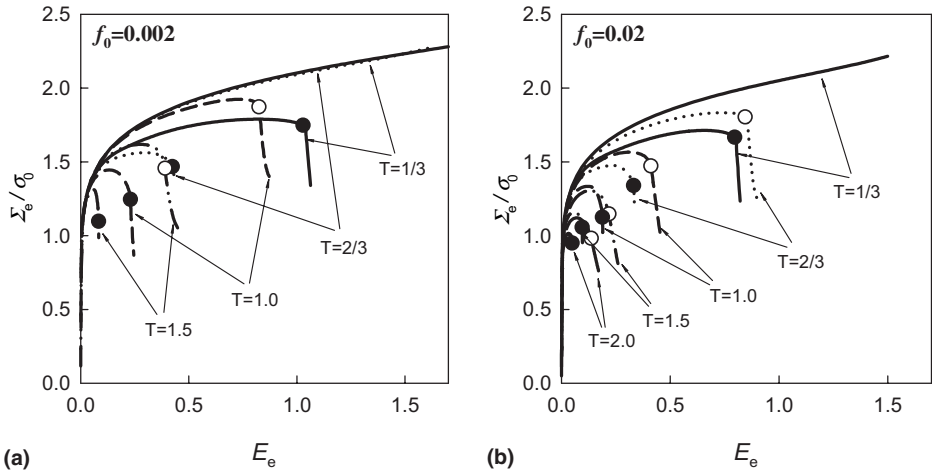

Fig. 4. Comparison of the macroscopic effective stress versus effective strain curves between models including and not including secondary voids. The open circles denote the onset of coalescence for models where secondary voids are not taken into account. The filled circles represent the onset of coalescence for models where nucleation ($f_N = 0.04$, $\varepsilon_N = 0.1$ and $s_N = 0.05$), growth and coalescence of secondary voids are accounted for. (a) $f_0 = 0.002$ and (b) $f_0 = 0.02$.

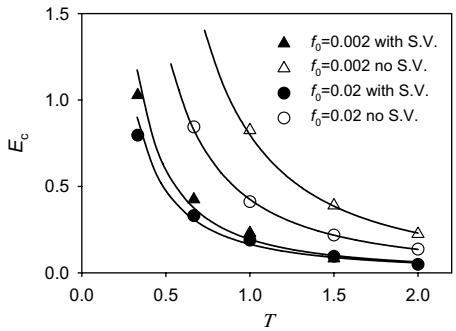

Fig. 5. Variation of E_c with T for fixed θ-value ($\theta = -30°$).

This suggests that the relationship between E_c and T may be characterized by exponential or inverse power-law functions. Fig. 5 also shows that E_c decreases with f_0, the initial volume fraction of the primary void.

2.4. Material failure surface as a function of the stress triaxiality ratio and the Lode angle

The calculations presented above only consider the case where the macroscopic stress state subjected by the RMV is axisymmetric, i.e., $\Sigma_2 \geqslant \Sigma_1 = \Sigma_3$ ($\theta = -30°$). However, as shown in Kim et al. (2004), the Lode angle has significant effect on void growth and coalescence and material failure. Fig. 6 shows the deformed shapes of the RMV under a series of macroscopic stress states having the same triaxiality ratio ($T = 1$) but different Lode angles. The θ values considered represent a variation of stress states from axisymmetric tension ($\theta = -30°$) to biaxial tension ($\theta = 30°$).

Fig. 7 compares the matrix plastic strain distribution for different Lode angles, $\theta = -30°$, 0°, and 30°. Here, the macroscopic stress triaxiality ratio is taken as $T = 1.5$, the initial volume fraction of the primary void is

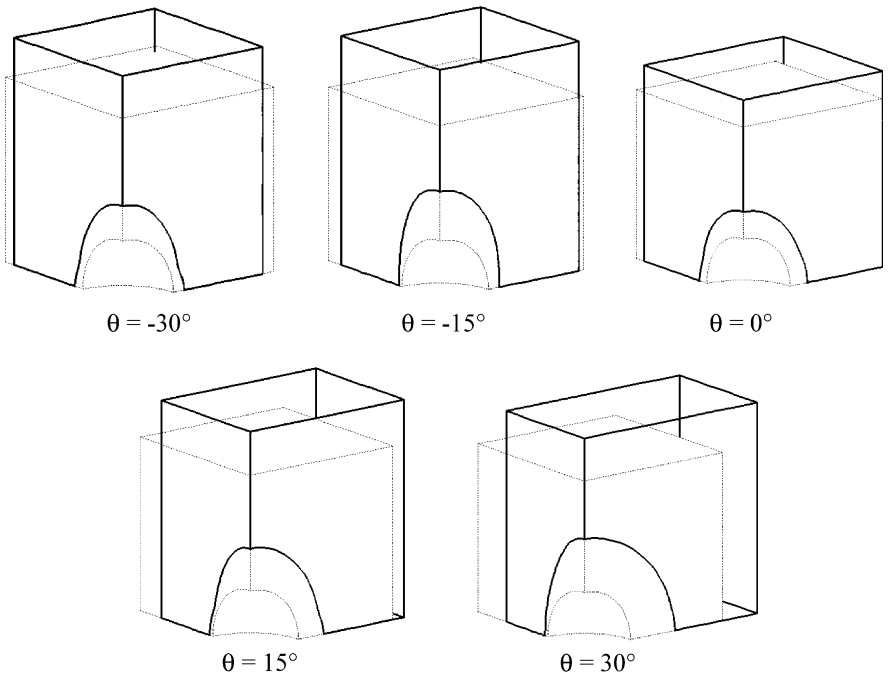

Fig. 6. Deformed shapes of the RMV under a series of macroscopic stress states having the same triaxiality ratio ($T = 1$) but different Lode angles.

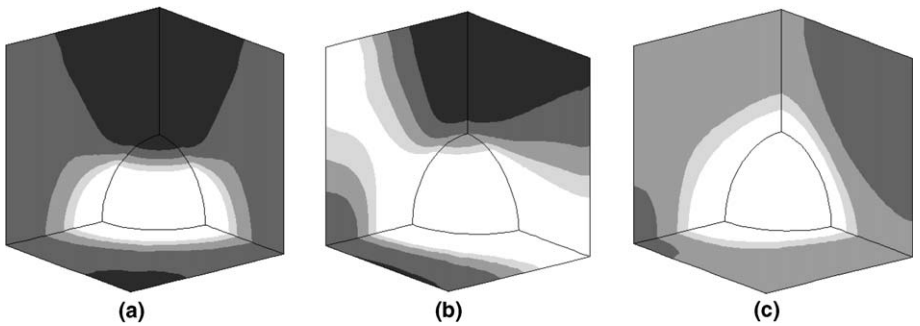

Fig. 7. Comparison of the matrix plastic strain distribution for three cases having different Lode angles. Here, $T = 1.5$ and $f_0 = 0.02$. (a) $\theta = -30°$, (b) $\theta = 0°$, and (c) $\theta = 30°$.

taken as $f_0 = 0.02$, and nucleation, growth and coalescence of secondary voids are taken into account. For $\theta = -30°$, high plastic strain occurs in the transverse plane perpendicular to the major loading direction (Σ_2). For $\theta = 0°$, high plastic strain occurs in the transverse plane as well as the plane having a 45° angle with the Σ_2-direction. For $\theta = 30°$, high plastic strain occurs in planes perpendicular to both major loading directions (Σ_2 and Σ_3).

Fig. 8 shows the volume fraction distribution of the secondary voids for the three cases considered in Fig. 7. The volume fraction of the secondary voids is attributed to both void nucleation (controlled by the plastic strain) and void growth (controlled by the stress triaxiality). The contour of the secondary void volume fraction equal to 0.1 can be used to indicate ligament material failure (Tvergaard and Needleman, 1984; Needleman and Tvergaard, 1987; Gao et al., 1998a,b). Due to the combined effects of the plastic strain and the local stress triaxiality, failure occurs in the transverse plane perpendicular to Σ_2 for the $\theta = -30°$ case, in the transverse plane as well as a slant plane for the $\theta = 0°$ case, and in two planes perpendicular to Σ_2 and Σ_3, respectively for the $\theta = 30°$ case.

Fig. 9 compares the stress–strain behavior of the RMV subjected to the same stress triaxiality ratio, $T = 1.5$, but different Lode angles, $\theta = -30°$, $-15°$, 0°, 15°, and 30°. In Fig. 9, curves having open symbols are for cases without secondary voids and curves having filled symbols are for cases with secondary voids being included. The symbols indicate the onset of coalescence. In general, a delay of coalescence is observed as the value of the Lode angle increases, i.e., E_c increases with θ.

The above analyses are carried out for a series of stress triaxiality ratios and the resulted variation of E_c as a function of T and θ is revealed in Fig. 10. Fig. 10 shows that E_c decreases with T but increases with θ. It is

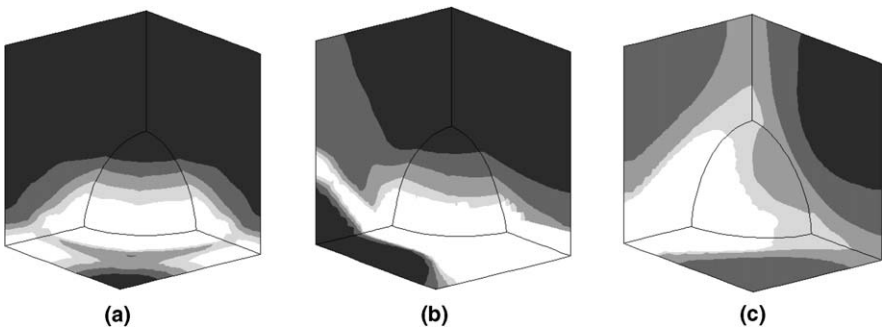

Fig. 8. Comparison of the volume fraction distribution of the secondary voids for three cases having different Lode angles. Here, $T = 1.5$ and $f_0 = 0.02$. (a) $\theta = -30°$, (b) $\theta = 0°$, and (c) $\theta = 30°$.

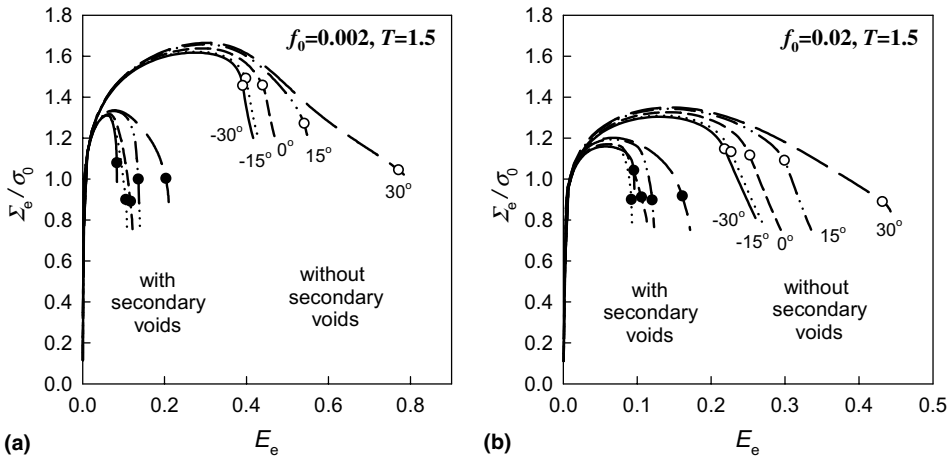

Fig. 9. Comparison of the stress–strain behavior of the RMV subjected to the same stress triaxiality ratio, $T = 1.5$, but different Lode angles, $\theta = -30°$, $-15°$, 0°, 15°, and 30°. The symbols indicate the onset of coalescence. (a) $f_0 = 0.002$ and (b) $f_0 = 0.02$.

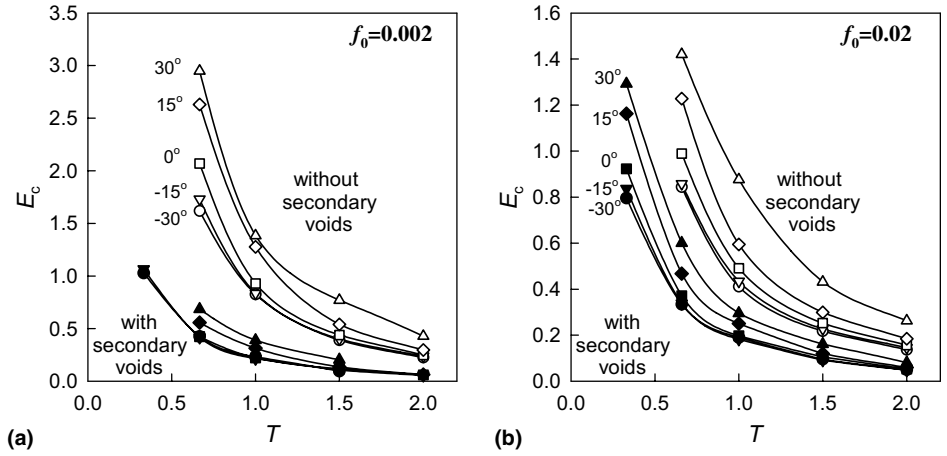

Fig. 10. Variation of E_c as a function of T and θ. (a) $f_0 = 0.002$ and (b) $f_0 = 0.02$.

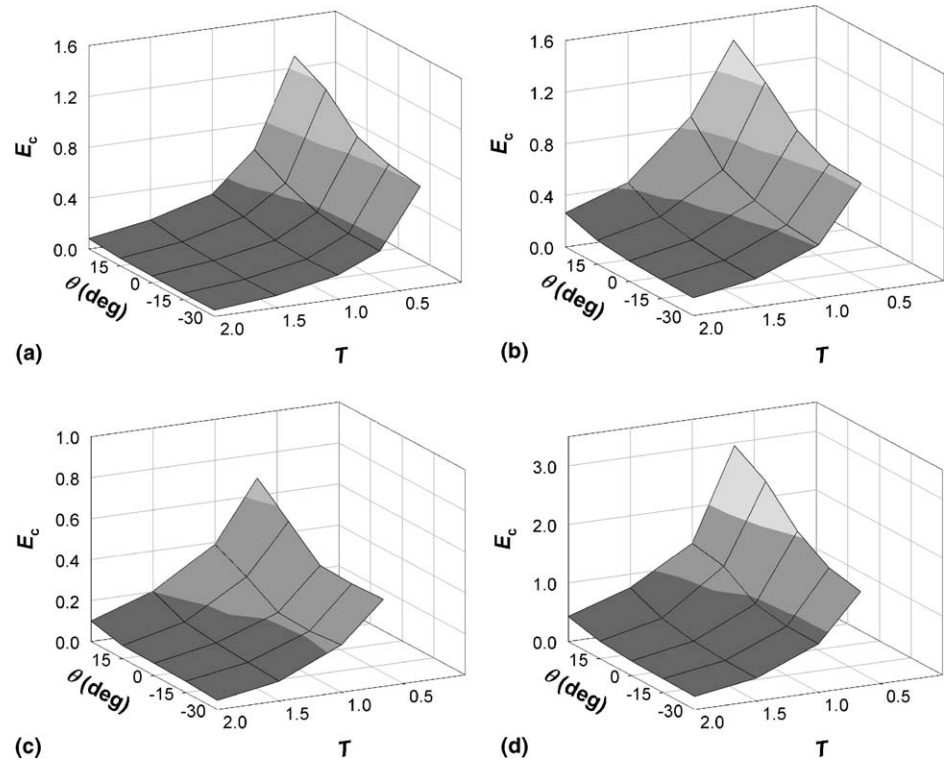

Fig. 11. Material failure surface in terms of E_c as a function of T and θ. (a) $f_0 = 0.02$ with secondary voids, (b) $f_0 = 0.02$ and no secondary voids, (c) $f_0 = 0.002$ with secondary voids, and (d) $f_0 = 0.002$ and no secondary voids.

interesting to note that the curves for $\theta = -30°$, $-15°$, and $0°$ are very close, which suggests that E_c is almost independent of θ when θ takes negative values. Results displayed in Fig. 10 can be represented as 3D plots as shown in Fig. 11. The surface representing function $E_c(T, \theta)$ is referred to as the failure surface. Fig. 11(a)–(d) display the material failure surface for cases $f_0 = 0.02$ with and without secondary voids and $f_0 = 0.002$ with and without secondary voids, respectively.

2.5. Effect of void shape

In previous sections, the initial shape of the primary void is assumed to be spherical. This section examines the effect of the initial void shape on the failure process. Besides the spherical shape, two other shapes, the prolate shape and the oblate shape, are considered. Fig. 12 shows the geometrical representation of the voids. The prolate and oblate voids are assumed to be axisymmetric about the y-axis and an initial aspect ratio is defined as $W_0 = R_{0y}/R_{0x}$. Therefore, $W_0 = 1$ corresponds to the spherical shape, $W_0 > 1$ corresponds to the prolate shape, and $W_0 < 1$ corresponds to the oblate shape. For the analyses performed in this section, nucleation, growth and coalescence of secondary voids are always included.

Fig. 13(a) compares the macroscopic stress–strain curves of the RMV having different initial void shapes. The initial void volume fraction is taken as $f_0 = 0.002$ and the initial void aspect ratio is chosen to be $W_0 = 4$ for the prolate void and $W_0 = 0.25$ for the oblate void. In Fig. 13(a), the RMVs are loaded according to $T = 1$ and $\theta = -30°$. The symbols indicate the onset of coalescence. It is not surprising that the critical equivalent strain is largest when the initial void is prolate and smallest when the initial void is oblate, i.e., E_c decreases with W_0. With θ being fixed at $-30°$, Fig. 13(b) shows similar trends of the E_c versus T relationships for the prolate, spherical and oblate voids with the Lode angle fixed at $\theta = -30°$. After conducting a series analyses for an array of T and θ values, the failure surfaces, $E_c(T, \theta)$, can be generated for the prolate and oblate void shapes, Fig. 14. These failure surfaces have similar features as those for spherical void described previously.

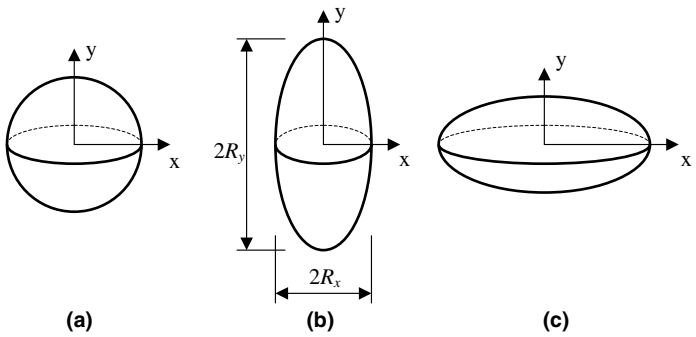

Fig. 12. Geometric representation of voids: (a) spherical void, (b) prolate void, and (c) oblate void.

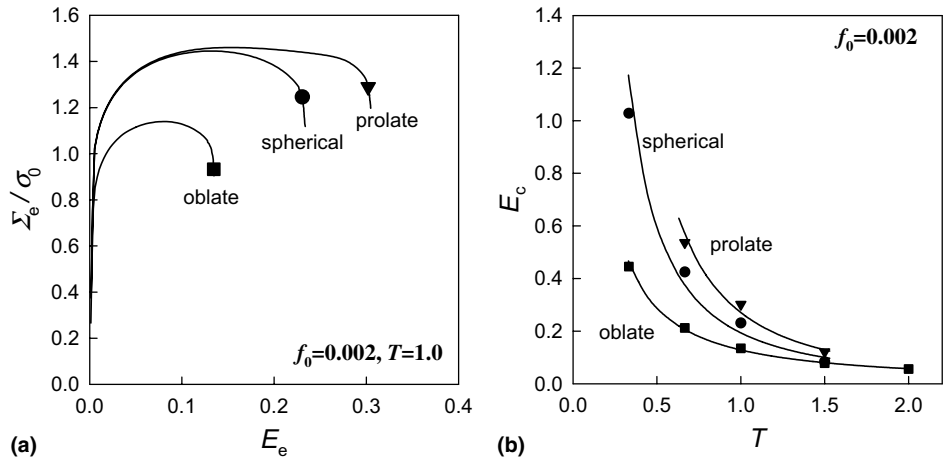

Fig. 13. (a) Comparison of the macroscopic stress–strain curves for the prolate ($W_0 = 4$), spherical ($W_0 = 1$) and oblate voids ($W_0 = 0.25$). The RMVs are loaded according to $T = 1$ and $\theta = -30°$. (b) Comparison of the E_c versus T relationships for different void shapes with the Lode angle fixed at $\theta = -30°$.

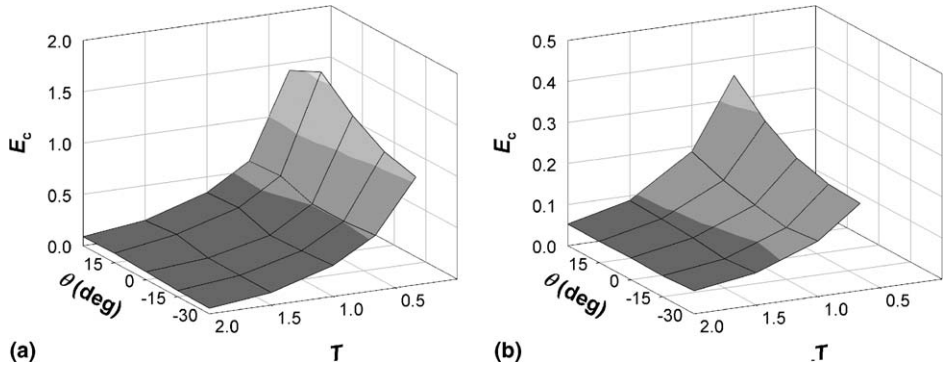

Fig. 14. Failure surfaces in terms of E_c as a function of T and θ for materials containing (a) prolate voids ($W_0 = 4$), and (b) oblate voids ($W_0 = 0.25$). Here, the initial void volume fraction is $f_0 = 0.002$ and nucleation, growth and coalescence of secondary voids are considered.

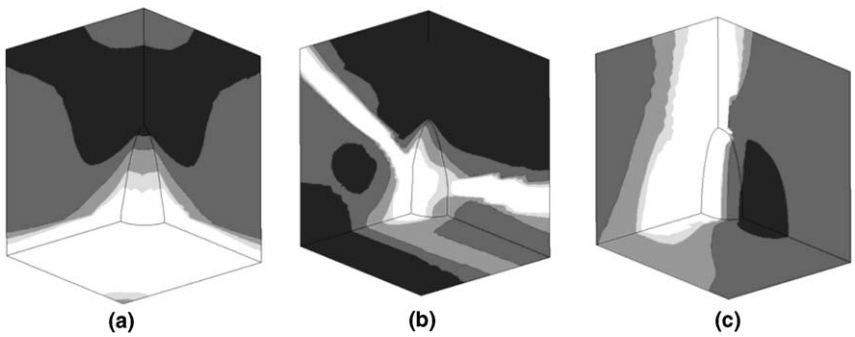

Fig. 15. Comparison of the volume fraction distribution of the secondary voids for three cases having different Lode angles. Here, $T = 1.5$ and the primary void is prolate with $W_0 = 4$ and $f_0 = 0.002$. (a) $\theta = -30°$, (b) $\theta = 0°$, and (c) $\theta = 30°$.

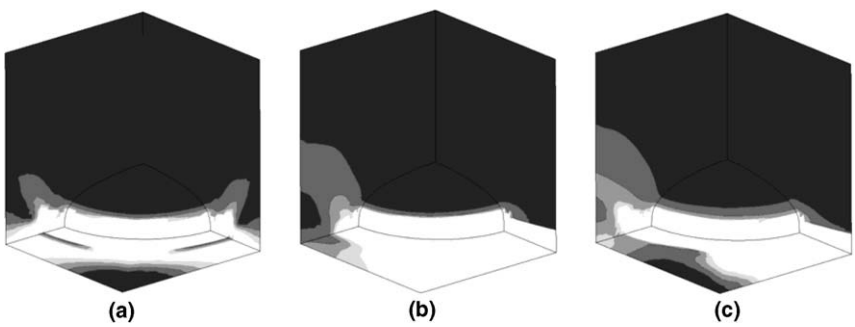

Fig. 16. Comparison of the volume fraction distribution of the secondary voids for three cases having different Lode angles. Here, $T = 1.5$ and the primary void is oblate with $W_0 = 0.25$ and $f_0 = 0.002$. (a) $\theta = -30°$, (b) $\theta = 0°$, and (c) $\theta = 30°$.

Fig. 15 shows the distributions of the secondary void volume fraction in the RMV containing an initially prolate void ($f_0 = 0.002$ and $W_0 = 4$) and loaded with $T = 1.5$ and $\theta = -30°$, 0°, and 30°. It can be see that material failure occurs at the plane perpendicular to Σ_2 when $\theta = -30°$, at a slant plane when $\theta = 0°$, and at the plane perpendicular to Σ_3 when $\theta = 30°$. On the other hand, if the initial void is oblate ($f_0 = 0.002$ and $W_0 = 0.25$) and the applied stress triaxiality is still $T = 1.5$, failure always occurs at the plane perpendicular to Σ_2 as shown in Fig. 16. The results displayed in Figs. 15 and 16 are very interesting and may be used to explain the different fracture modes exhibited by specimens of different orientations. For example, Dawicke

and Sutton (1993) and Sutton et al. (1995) conducted fracture tests of 2024-T3 aluminum plates and observed flat fracture surfaces for TL specimens in which the inclusion shape is oblate and a flat-to-slant transition of the fracture surfaces for LT specimens in which the inclusion shape is prolate.

3. Simulation of crack growth in thin panels of a 2024-T3 aluminum alloy

Dawicke and Newman (1997, 1998) performed extensive fracture tests on thin panels of a 2024-T3 aluminum alloy including tests of C(T) and M(T) specimens with crack planes in both the LT and TL orientations. The LT tests have been analyzed by Gullerud et al. (1999) using a crack tip opening angle (CTOA) criterion to govern crack growth and by Arun Roy and Dodds (2001) and Roychowdhury et al. (2002) using cohesive elements to model crack propagation. Here, we propose an approach to predict ductile crack growth by simulating the void growth and coalescence process. The test data of our interest are from LT specimens with a sheet thickness of 2.3 mm. The specimens have very stiff guide plates (coated with Teflon tape) to constrain out-of-plane (buckling) displacements. In the L orientation, the 2024-T3 sheet material used in the experiments has a yield stress of 345 MPa, Young's Modulus of 71.3 GPa, and Poisson's ratio of 0.3. Table 1 lists the measured, uniaxial true stress versus logarithmic strain values for the material. Quantitative metallographic analyses were performed to determine the inclusion volume fraction, shape and average spacing. It is found that the inclusion volume fraction (f_0) is approximately 0.02, the average spacing between inclusions in the LT plane is about 50 μm, and in LT specimens, the inclusions can be approximated as prolate spheroids with $W_0 = 4$.

3.1. Modeling the void growth process

Because the fracture specimens contain non-spherical voids, we adopt the GLD porous plasticity model (Gologanu et al., 1993, 1994, 1995) to describe the void growth behavior and the macroscopic plastic response. The void geometry is illustrated in Fig. 12. The yield function of the void-containing material can be expressed as

$$\Phi = \frac{C}{\bar{\sigma}^2}\|\boldsymbol{\Sigma}' + \eta\Sigma_{\mathrm{h}}\mathbf{X}\|^2 + 2q(g+1)(g+f)\cosh\left(\kappa\frac{\Sigma_{\mathrm{h}}}{\bar{\sigma}}\right) - (g+1)^2 - q^2(g+f)^2 = 0, \tag{9}$$

where Σ_{ij} are the macroscopic stress components, f represents the void volume fraction, S is the shape parameter defined as $S = \ln(W)$ with $W = R_y/R_x$, and $\bar{\sigma}$ is the yield stress of the matrix material. In Eq. (9), $\|\,\|$ denotes the von Mises norm, $\boldsymbol{\Sigma}'$ is the deviatoric stress tensor, Σ_{h} is the generalized hydrostatic stress defined by $\Sigma_{\mathrm{h}} = \alpha_2(\Sigma_{xx} + \Sigma_{zz}) + (1-\alpha_2)\Sigma_{yy}$, $\mathbf{X}$ is a tensor defined as $\mathbf{X} = (2/3)\boldsymbol{e}_y \otimes \boldsymbol{e}_y - (1/3)\boldsymbol{e}_x \otimes \boldsymbol{e}_x - (1/3)\boldsymbol{e}_z \otimes \boldsymbol{e}_z$, where $(\boldsymbol{e}_x, \boldsymbol{e}_y, \boldsymbol{e}_z)$ is an orthogonal basis with $\boldsymbol{e}_y$ parallel to the axisymmetric axis of the void, and $\otimes$ denotes tensor product. The parameters C, η, g, κ, and α_2 are functions of f and S and the heuristic parameter q depends on initial void volume fraction, strain hardening exponent of the matrix material, S and the macroscopic stress triaxiality factor T.

The evolution equation for f is the same as Eq. (8) and the derivation of the evolution equation for S can be found in Gologanu et al. (1993, 1994). Pardoen and Hutchinson (2000, 2003) provide detailed descriptions and formulation for the GLD model. Kim and Gao (2005) developed a generalized approach to formulate the consistent tangent stiffness for complicated plasticity models. Using this approach, we implemented the GLD

Table 1
Measured true stress versus logarithmic strain curve for Al 2024-T3 (L orientation)

σ (MPa)	ε (logarithmic)
346	0.0048
395	0.015
448	0.039
519	0.095
567	0.148
587	0.182

model in ABAQUS via a user subroutine. See Kim and Gao (2005) for details of the numerical implementation of the GLD model.

3.2. A computational approach for the post-coalescence process

The GLD model described above governs the plastic behavior of the RMV during the void growth process. As the macroscopic effective strain (E_e) reaches E_c, void coalescence occurs and the RMV quickly loses its stress carrying capacity. We adopt the f^* function, introduced by Tvergaard and Needleman (1984), to account for the effects of rapid void coalescence at failure. After E_e reaches E_c, f is replaced by f^* in the GLD model, where

$$f^* = \begin{cases} f, & f \leqslant f_c \\ f_c + K(f - f_c), & f > f_c \end{cases}. \tag{10}$$

In Eq. (10), f_c is the void volume fraction at $E_e = E_c$, $K = (f_u - f_c)/f_c$, and f_u is the f^* value at zero stress. For prolate void, $f_u = 1/q$, and for oblate void, $f_u = (1 + g - gq)/q$. Since AQAQUS/Standard does not provide an element removal procedure, a modification to Eq. (10) is needed for numerical stability. Eq. (10) is employed until $f^* = 0.99 f_u$. Then an exponential function is used such that f^* gradually approaches to f_u (but can never reach f_u).

3.3. Model calibration

For the material considered here, f_0 is taken as 0.02. To predict crack growth, the function $E_c(T, \theta)$ needs to be determined. The results presented in Section 2 suggest that E_c is not sensitive to θ when θ takes negative values. We perform finite element analyses of the fracture specimens considered in this study and find the θ-values of the representative material volumes ahead of the crack front are in the range of $-15^\circ \leqslant \theta \leqslant 0^\circ$ (as will be shown in Fig. 20). Therefore, we treat E_c as a function of T only. Based on the previous results, we assume

$$E_c = \alpha(T)^\beta, \tag{11}$$

where α and β are two parameters need to be calibrated using experimental data. A recent study by Bao (2005) supports the power-law form of $E_c(T)$ function defined by Eq. (11). Bao conducted an experimental and numerical study of ductile failure of a 2024-T351 aluminum alloy using different tensile specimens including flat specimens, smooth round bars, notched bars and flat-grooved plates and found that the equivalent strain at failure versus the average stress triaxiality can be characterized by a function in the form of Eq. (11).

Two data points are needed to determine α and β. The uniaxial tension test provides one point, $T = 1/3$ and $E_c = 0.182$. Substitution of these values into (11) results in $\alpha = 0.182(3)^\beta$. The next step of the calibration process seeks to match the model predicted load versus crack propagation curve with the experimental measurements for the C(T) specimen. This step entails several finite element crack growth analyses of the C(T) specimen using different values of β.

The C(T) specimen has a width of 150 mm with $a/W = 0.33$, where a represents the initial crack length and W represents the specimen width. Due to symmetry, only 1/4 of the specimen needs to be modeled. Fig. 17 shows the quarter-symmetric finite element mesh of the C(T) specimen having 27,400 eight-node, isoparametric solid elements (with reduced integration). The mesh near the crack front has six layers with varying thickness to capture the stress gradient in the thickness direction, where the thickest elements are at the symmetry plane. The elements directly ahead of the crack front have uniform in-plane dimensions ($L_e = 50$ μm) and are governed by the GLD model. All other elements follow J_2 flow plasticity. Loading of the C(T) specimen is controlled by prescribing a displacement on a rigid pin through the hole.

Fig. 18 shows the comparison between the model predicted load versus crack growth curve with the experimental measurements (two sets of experimental data) for different choices of α and β, where the lines represent model predictions and the symbols denote experimental measurements. Here, Δa represent the amount of crack growth measured at the free surface. In the numerical model, the propagating crack front is defined

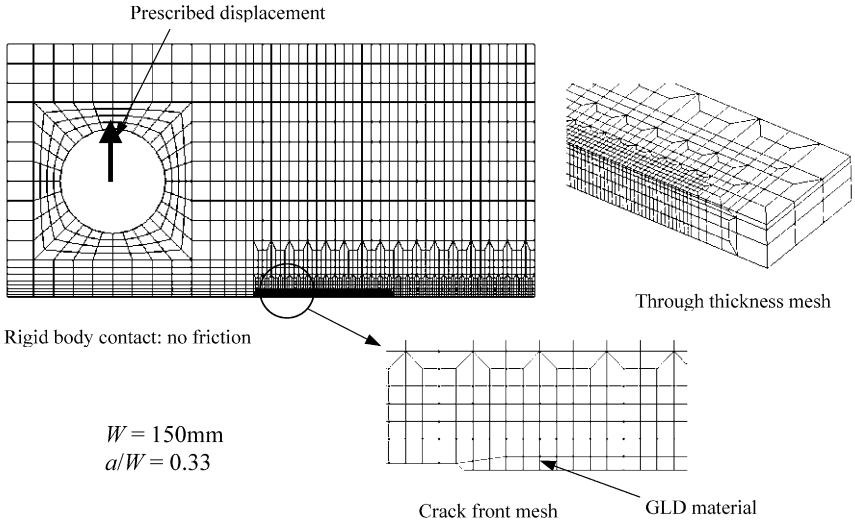

Fig. 17. A quarter-symmetric finite element mesh for the C(T) specimen. The mesh near the crack front has six layers with varying thickness to capture the stress gradient in the thickness direction. The elements directly ahead of the crack front have uniform in-plane dimensions ($L_e = 50$ μm) and are governed by the GLD model.

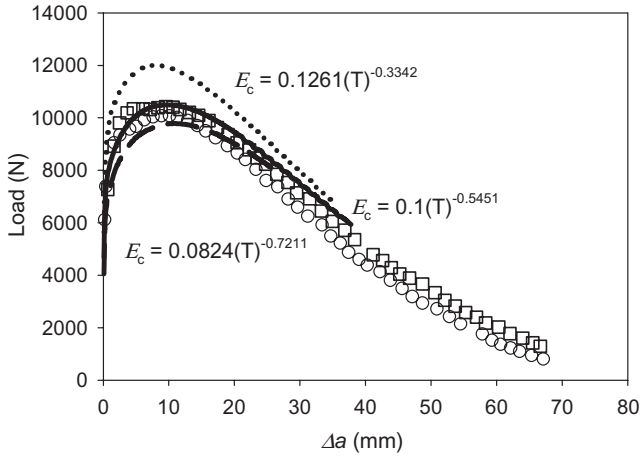

Fig. 18. Comparison of the model predicted load versus crack growth curve with the experimental measured data (symbols) showing the choice of $\alpha = 0.1$ and $\beta = -0.5451$ (solid line) results in a best fit to the experimental data.

by the elements which have reached the failure strain E_c. From Fig. 18, it can be seen that the choice of $\alpha = 0.1$ and $\beta = -0.5451$ (solid line) results in the best fit to the experimental data. Therefore, these values are the calibrated values for α and β and will be used to predict crack growth in other fracture specimens.

Fig. 19 displays the predicted crack front showing the interior part tunneling ahead. This agrees with the experimental observations. Fig. 20 shows the variations of the Lode angle (θ) of the GLD elements with crack growth (Δa) for all six rows of GLD elements, where row 1 denotes elements in the middle of the specimen and row 6 denotes elements at the free surface. It can be seen that θ is always in the range of $-15° \leqslant \theta \leqslant 0°$.

3.4. Prediction of crack growth in M(T) specimens

The calibrated computational model is employed to predict the crack extension behavior of M(T) specimens. Fig. 21(a) shows a 1/8-symmetric finite element mesh for a 300 mm M(T) specimen. The mesh near

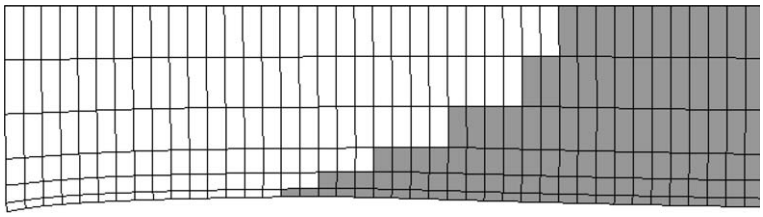

Fig. 19. Predicted crack front showing the interior part tunneling ahead.

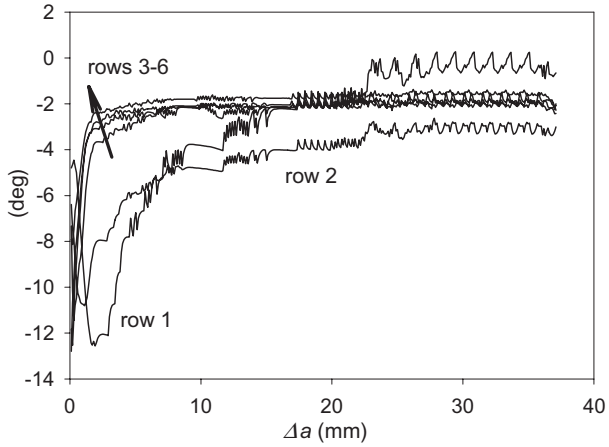

Fig. 20. Variations of θ with crack growth (Δa) for the GLD elements, where row 1 denotes elements in the middle of the specimen and row 6 denotes elements at the free surface.

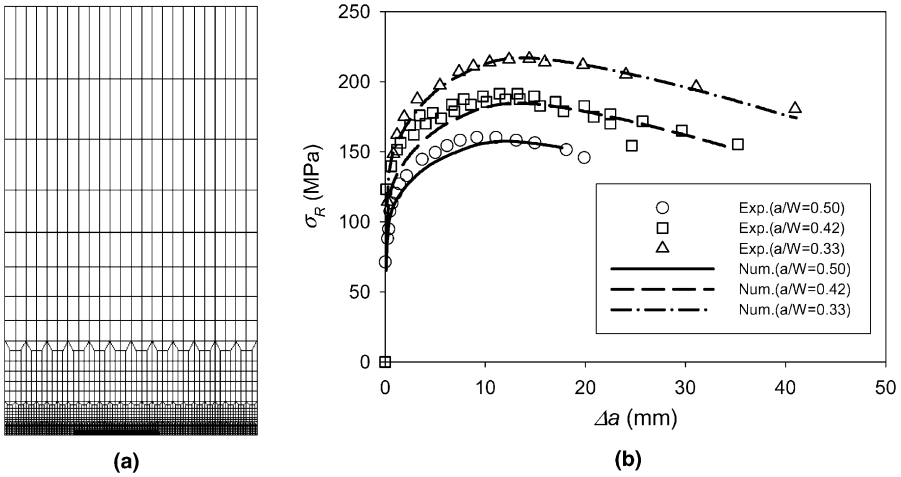

Fig. 21. (a) A typical, 1/8-symmetric finite element mesh for the M(T) specimen (front view). (b) Comparison of the model predicted load versus crack extension responses (lines) with experimental measurements (symbols).

the crack front are the same as used in the C(T) specimen. Three M(T) specimens with a/W ratios of 0.33, 0.42, and 0.5 are analyzed. The nominal remote stress, σ_R, characterizes the loading for these specimens. Fig. 21(b) compares the computed load versus crack extension responses with experimental measurements, showing very good agreement for all three cases. This serves as a verification of the proposed computational approach.

4. Concluding remarks

The critical strain at the onset of void coalescence depends on material flow properties and microstructural properties. It also depends on the stress state. Two stress parameters, the stress triaxiality ratio (T) and the Lode angle (θ) can be used to characterize the effect of the macroscopic stress state on the void growth and coalescence process in the representative material volume (RMV). We obtain the failure criterion for the RMV in terms of the macroscopic equivalent strain (E_c) as a function of T and θ by conducting systematic finite element analyses of the void-containing RMV subjected to different macroscopic stress states. A series of parameter studies are conducted to examine the effects of the shape and initial volume fraction of the primary void and nucleation, growth and coalescence of the secondary voids on the predicted failure surface $E_c(T,\theta)$. The following remarks can be made about the failure strain E_c:

(1) E_c decreases with T. The dependency of E_c on T is more pronounced in the low stress triaxiality range and saturates as T increases to high level.
(2) E_c increases with θ and the change in E_c becomes less sensitive to θ when $-30^\circ \leqslant \theta \leqslant 0^\circ$.
(3) E_c decreases with f_0, the initial volume fraction of the primary void.
(4) Nucleation, growth and coalescence of secondary voids accelerate the ligament failure process and reduce E_c.
(5) E_c increases with W_0, the aspect ratio of the primary void.

As an application, a numerical approach is proposed to predict ductile crack growth in thin panels of a 2024-T3 aluminum alloy, where the GLD porous plasticity model is used to describe the void growth process and a f^* function is employed to account for rapid material failure in the post-coalescence process. The critical strain at the onset of void coalescence is found to be a function of the stress triaxiality ratio only and a procedure to calibrate $E_c(T)$ is presented. The calibrated computational model accurately predicts crack extension in fracture specimens having various initial crack configurations.

Acknowledgements

This research was made possible through research funding provided by the Office of Naval Research (N00014-02-1-0423) and by the Ohio Board of Regents.

References

ABAQUS, 2004. ABAQUS/Standard User's Manual, Version 6.4, Hibbit, Karlsson and Sorensen Inc.
Aravas, N., McMeeking, R.M., 1985a. Finite element analysis of void growth near a blunting crack tip. J. Mech. Phys. Solids 33, 25–49.
Aravas, N., McMeeking, R.M., 1985b. Microvoid growth and failure in the ligament between a hole and blunt crack tip. Finite element analysis of void growth near a blunting crack tip. Int. J. Fract. 29, 21–38.
Arun Roy, Y., Dodds, R.H., 2001. Simulation of ductile crack growth in thin aluminum panels using 3D surface cohesive elements. Int. J. Fact. 110, 21–45.
Bao, Y., 2005. Dependence of ductile crack formation in tensile tests on stress triaxiality, stress and strain ratios. Eng. Fract. Mech. 72, 505–522.
Bao, Y., Wierzbicki, T., 2004a. A comparative study on various ductile crack formation criteria. J. Eng. Mater. Tech. 26, 314–324.
Bao, Y., Wierzbicki, T., 2004b. On fracture locus in the equivalent strain and stress triaxiality space. Int. J. Mech. Sci. 46, 81–98.
Benzerga, A.A., 2002. Micromechanics of coalescence in ductile fracture. J. Mech. Phys. Solids 50, 1331–1362.
Benzerga, A.A., Besson, J., Pineau, A., 1999. Coalescence-controlled anisotropic ductile fracture. J. Eng. Mater. Technol. 121, 221–229.
Benzerga, A.A., Besson, J., Pineau, A., 2004. Anisotropic ductile fracture—Part II: theory. Acta Mater. 52, 4639–4650.
Chu, C.C., Needleman, A., 1980. Void nucleation effects in biaxially stretched sheets. J. Eng. Mater. Technol. 102, 249–256.
Dawicke, D.S., Newman, J.C., 1997. Evaluation of fracture parameters for prediction residual strength of multi-site damage cracking. In: Proceedings from the First Joint NASA/FAA/DoD Conference on Aging Aircraft.
Dawicke, D.S., Newman, J.C., 1998. Residual strength predictions for multiple site damage cracking using a three-dimensional finite element analysis and a CTOA criterion. In: Panontin, T.L., Sheppard, S.D. (Eds.), Fatigue and Fracture Mechanics, vol. 29, ASTM STP 1332, ASTM, Philadelphia, PA, pp. 815–829.
Dawicke, D.S., Sutton, M.A., 1993. Crack-tip-opening angle measurements and crack tunneling under stable tearing in thin sheet 2024-T3 aluminum alloy. NASA-CR-191523.

Faleskog, J., Shih, C.F., 1997. Micromechanics of coalescence—I. synergistic effects of elasticity, plastic yielding and multi-size-scale voids. J. Mech. Phys. Solids 45, 21–50.

Faleskog, J., Gao, X., Shih, C.F., 1998. Cell model for nonlinear fracture analysis—I. Micromechanics calibration. Int. J. Fract. 89, 355–373.

Gao, X., Faleskog, J., Shih, C.F., 1998a. Cell model for nonlinear fracture analysis—II. Fracture-process calibration and verification. Int. J. Fract. 89, 375–398.

Gao, X., Faleskog, J., Shih, C.F., Dodds, R.H., 1998b. Ductile tearing in part-through cracks: experiments and cell-model predictions. Eng. Fract. Mech. 59, 761–777.

Gao, X., Wang, T., Kim, J., 2005. On ductile fracture initiation toughness: effects of void volume fraction, void shape and void distribution. Int. J. Solids Struct. 42, 5097–5117.

Garrison, W.M., Moody, N.R., 1987. Ductile fracture. J. Phys. Chem. Solids 48, 1035–1047.

Gologanu, M., Leblond, J.B., Devaux, J., 1993. Approximate models for ductile metals containing nonspherical voids—case of axisymmetric prolate ellipsoidal cavities. J. Mech. Phys. Solids 41, 1723–1754.

Gologanu, M., Leblond, J.B., Devaux, J., 1994. Approximate models for ductile metals containing nonspherical voids—case of axisymmetric oblate ellipsoidal cavities. J. Eng. Mater. Tech. 116, 290–297.

Gologanu, M., Leblond, J.B., Perrin, G., Devaux, J., 1995. Recent extensions of Gurson's model for porous ductile metals. In: Suquet, P. (Ed.), Continuum Micromechanics. Springer-Verlag, Berlin.

Gullerud, A.S., Dodds, R.H., Hampton, R.W., Dawicke, D.S., 1999. 3D modeling of ductile crack growth in thin sheet metals: computational aspects and validation. Eng. Fract. Mech. 63, 347–374.

Gurson, A.L., 1977. Continuum of ductile rupture by void nucleation and growth—Part I: Yield criteria and flow rules for porous ductile media. J. Eng. Mater. Tech. 99, 2–55.

Kim, J., Gao, X., 2005. A generalized approach to formulate the consistent tangent stiffness in plasticity with application to the GLD porous material model. Int. J. Solids Struct. 42, 103–122.

Kim, J., Gao, X., Srivatsan, T.S., 2003. Modeling of crack growth in ductile solids: a three-dimensional analysis. Int. J. Solids Struct. 40, 7357–7374.

Kim, J., Gao, X., Srivatsan, T.S., 2004. Modeling of void growth in ductile solids: effects of stress triaxiality and initial porosity. Eng. Fract. Mech. 71, 379–400.

Koplik, J., Needleman, A., 1988. Void growth and coalescence in porous plastic solids. Int. J. Solids Struct. 24, 835–853.

Needleman, A., Tvergaard, V., 1987. An analysis of ductile rupture modes at a crack tip. J. Mech. Phys. Solids 35, 151–183.

Pardoen, T., Hutchinson, J.W., 2000. An extended model for void growth and coalescence. J. Mech. Phys. Solids 48, 2467–2512.

Pardoen, T., Hutchinson, J.W., 2003. Micromechanics-based model for trends in toughness of ductile metals. Acta Mater. 51, 133–148.

Roychowdhury, S., Arun Roy, Y., Dodds, R.H., 2002. Ductile tearing in thin aluminium panels: experiments and analyses using large-displacement, 3-D surface cohesive elements. Eng. Fract. Mech. 69, 983–1002.

Sutton, M.A., Dawicke, D.S., Newman, J.C., 1995. Orientation effects on the measurement and analysis of critical CTOA in an aluminum alloy sheet. In: Reuter, W.G., Underwood, J.H., Newman, J.C. (Eds.), Fracture Mechanics, vol. 26, ASTM STP 1256, Philadelphia, PA, pp. 243–255.

Tvergaard, V., Hutchinson, J.W., 2002. Two mechanisms of ductile fracture: void by void growth versus multiple void interaction. Int. J. Solids Struct. 39, 3581–3597.

Tvergaard, V., Needleman, A., 1984. Analysis of the cup-cone fracture in a round tensile bar. Acta Metall. 32, 157–169.

Tvergaard, V., 1981. Influence of voids on shear band instabilities under plane strain conditions. Int. J. Fract. 17, 389–407.

Tvergaard, V., 1982. On Localization in ductile materials containing spherical voids. Int. J. Fract. 18, 237–252.

Van Stone, R., Cox, T., Low, J., Psioda, J., 1985. Microstructural aspects of fracture by dimpled rupture. Int. Metals Rev. 30, 157–179.

Wierzbicki, T., Xue, L., 2005. On the effect of the third invariant of the stress deviator on ductile fracture. Technical Report, Impact and Crashworthiness Lab, MIT.

Xia, L., Shih, C.F., Hutchinson, J.W., 1995. Computational approach to ductile crack growth under large scale yielding conditions. J. Mech. Phys. Solids 43, 389–413.

Zhang, Z.L., Thaulow, C., Odegard, J., 2000. A complete Gurson model approach for ductile fracture. Eng. Fract. Mech. 67, 155–168.